



Hierarchical analysis of spreading dynamics in complex systems

Aparimit Kasliwal¹ | Abdullah Alhadlaq¹ | Ariel Salgado^{2,3} |
Auroop R. Ganguly^{4,5} | Marta C. González^{1,3,6}

¹Department of Civil and Environmental Engineering, University of California Berkeley, Berkeley, California, USA

²Calculus Institute, University of Buenos Aires - CONICET, Buenos Aires, Argentina

³Department of City and Regional Planning, University of California Berkeley, Berkeley, California, USA

⁴Pacific Northwest National Laboratory, Washington, USA

⁵Department of Civil and Environmental Engineering, Northeastern University, Boston, Massachusetts, USA

⁶Energy Technologies Area, Lawrence Berkeley National Laboratory, Berkeley, California, USA

Correspondence

Marta C. González, Department of Civil and Environmental Engineering, University of California Berkeley, Berkeley, CA, USA.
Email: martag@berkeley.edu

Funding information

US DoD SERDP Networked Infrastructure under Compound Extremes (NICE), Grant/Award Number: RC20-1183

Abstract

Modeling spreading dynamics on spatial networks is crucial to addressing challenges related to traffic congestion, epidemic outbreaks, efficient information dissemination, and technology adoption. Existing approaches include domain-specific agent-based simulations, which offer detailed dynamics but often involve extensive parameterization, and simplified differential equation models, which provide analytical tractability but may abstract away spatial heterogeneity in propagation patterns. As a step toward addressing this trade-off, this work presents a hierarchical multiscale framework that approximates spreading dynamics across different spatial scales under certain simplifying assumptions. Applied to the Susceptible-Infected-Recovered (SIR) model, the approach ensures consistency in dynamics across scales through multiscale regularization, linking parameters at finer scales to those obtained at coarser scales. This approach constrains the parameter search space, and enables faster convergence of the model fitting process compared to the non-regularized model. Using hierarchical modeling, the spatial dependencies critical for understanding system-level behavior are captured while mitigating the computational challenges posed by parameter proliferation at finer scales. Considering traffic congestion and COVID-19 spread as case studies, the calibrated fine-scale model is employed to analyze the effects of perturbations and to identify critical regions and connections that disproportionately influence system dynamics. This facilitates targeted intervention strategies and provides a tool for studying and managing spreading processes in spatially distributed sociotechnical systems.

1 | INTRODUCTION

The study of spreading phenomena on complex spatial networks has emerged as a critical research area, particularly for understanding and managing processes like disease transmission through social contacts and traffic

congestion propagation on road networks. A foundational framework for modeling such processes is the compartmental SIR (Susceptible-Infected-Recovered) model, which was first introduced by O. Kermack and McKendrick (1927). In recent years, the classical SIR model has been extended in various directions to better reflect

This is an open access article under the terms of the [Creative Commons Attribution-NonCommercial-NoDerivs](https://creativecommons.org/licenses/by-nc-nd/4.0/) License, which permits use and distribution in any medium, provided the original work is properly cited, the use is non-commercial and no modifications or adaptations are made.

© 2025 The Author(s). *Computer-Aided Civil and Infrastructure Engineering* published by Wiley Periodicals LLC on behalf of Editor.



real-world complexities, including spreading on scale-free networks (Pastor-Satorras & Vespignani, 2001), metapopulation dynamics (Colizza et al., 2007), and multilayer networks (De Domenico et al., 2016), significantly enhancing its applicability to a wide range of spreading phenomena.

Within the specific context of transportation networks, traffic congestion spreading has recently been studied as a dynamical process. Formal contagion-style models describe congestion propagation analogously to epidemics (Kozhabeck et al., 2024; Saberi et al., 2020). Complementary studies examine how navigation and routing choices shape the spread of congestion (Bagabaldo et al., 2024; Zhang et al., 2022), and engineering models address work-zone capacity and queue delay (Jiang & Adeli, 2004). Previous research has also explored its progression toward network-level collapse (Olmos et al., 2018), including as a percolation process in networks (Ambühl et al., 2023). Several works such as Li et al. (2017) and Chen et al. (2020) have also studied the spread of traffic congestion through network-based contagion models, while Saberi et al. (2020) demonstrated the spread of traffic congestion behaves similarly to an epidemic process. Another work (Bagabaldo et al., 2024) further explored the impact of modern navigation apps on traffic congestion spread through contagion-based models. These prior efforts have contributed to a growing understanding of how congestion can emerge, propagate, and impact network performance under various conditions. However, many contagion-based studies tend to either represent large areas as aggregated nodes for the network representation, or focus on highly detailed street-level interactions, with fewer efforts examining intermediate spatial scales. In settings where congestion patterns vary across different regions of a road network, modeling approaches that explicitly account for such spatial heterogeneity may offer useful additional insights at the system level.

In parallel, predictive urban traffic models increasingly leverage deep learning and graph neural networks to maximize forecasting accuracy, including deep marked graph process models for citywide congestion forecasting (Zhang et al., 2023), multitask graph metro flow prediction (Zhao et al., 2025), and Bayesian physics-informed traffic state prediction with quantified uncertainty (Ding et al., 2025). In contrast, this work further develops the parsimonious and interpretable SIR model to capture via a hierarchical regularization framework that links parameters across spatial scales, enabling stable, data-efficient, and computationally scalable inference while preserving mechanistic clarity.

Representing spatial heterogeneity highlights a broader trade-off in current approaches to analyzing road network resilience—balancing model simplicity with spatial granularity. While microscopic agent-based models have

revealed critical vulnerabilities by quantifying the influence of specific road links (Ganin et al., 2017; Smith et al., 2014), city-scale and empirical ABM investigations highlight broader planning and robustness implications (Boeing & Ha, 2024; Chen et al., 2020), existing compartmental model-based frameworks either treat an entire region as one single aggregated system (Saberi et al., 2020), or explicitly model the spread of congestion at the individual street level (Kozhabeck et al., 2024). The former approach reduces complexity to effectively only two key parameters but overlooks spatial heterogeneity in congestion spread, while the latter captures specific street-network topology but requires extensive parameterization for large regions such as the San Francisco Bay Area. A similar modeling challenge arises in the context of infectious disease transmission, where mobility-driven network models have been used to capture spatial and demographic heterogeneity in the spread of COVID-19 (Chang et al., 2020), highlighting the importance of incorporating network structure when analyzing system-level dynamics.

Motivated by these considerations, a hierarchical multiscale framework is developed to approximate spreading dynamics across spatial scales while maintaining modeling consistency across different levels of granularity encompassed by these scales. This approach leverages recent advances in dimension reduction of complex systems through mean-field approximation, which has shown success in analyzing network resilience (Gao et al., 2016; Gao, 2024) and modeling multi-scale dynamics (González & Barabási, 2007; Salgado et al., 2024). Similar techniques have been applied to analyze phase transitions in dynamical systems (Thibeault et al., 2024) and critical transitions in coupled networks (Tu et al., 2021). Hierarchical Bayesian models have been used to predicting other spreading processes (Wikle, 2003). The proposed framework creates a hierarchical structure where smaller regions at finer scales are linked to their corresponding larger, so-called parent regions at coarser scales through a two-way process as indicated in Figure 1a. Although modeling at finer scales can offer improved spatial resolution, it often presents challenges such as overparameterization and non-uniqueness in parameter estimation. To help mitigate these issues, a regularization approach is introduced that incorporates information from coarser scales to inform parameter estimation at finer levels, providing a potential path toward more stable inference when data availability is limited.

This framework is exemplified through two distinct case studies: traffic congestion spreading on street networks and COVID-19 infection spreading in US counties during the Omicron variant peak (Saberi et al., 2020; Stolerman et al., 2015). Though both processes are linked to mobility

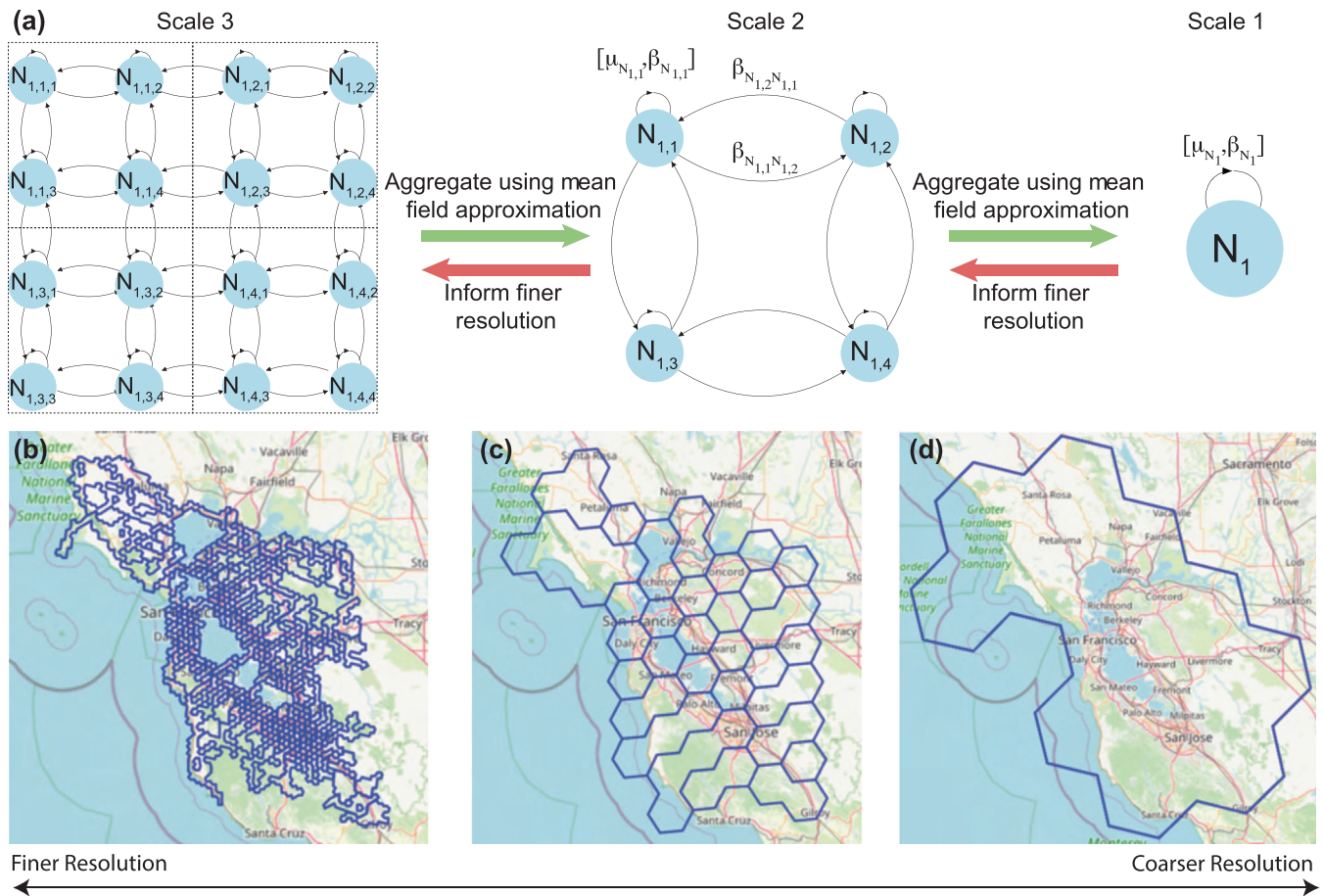


FIGURE 1 Hierarchical representation of multiscale modeling framework. (a) Conceptual illustration of three hierarchical scales showing parameter relationships. Nodes at finer scales are aggregated to inform coarser scale dynamics, while coarser scale parameters inform parameter estimation at finer scales through regularization. (b–d) Visualization of the system for traffic congestion modeling across three spatial scales. Network connectivity between nodes at each scale is governed by the presence of connecting road links between their respective regions.

patterns (Balcan et al., 2009; Gallotti et al., 2024), they operate at different scales and exhibit different spatial patterns. Phenomena modeled with contagion models, such as technology adoption (Lengyel et al., 2020; Toole et al., 2012) and information diffusion (Bettencourt et al., 2006; Rodrigues, 2016), can also be captured by this framework. From a network science perspective, this approach provides a balanced solution between model complexity and spatial resolution, while from an applications perspective, it enables targeted intervention strategies while maintaining computational efficiency. The influence between neighboring regions is quantified by measuring the impacts of an induced perturbation in the system, demonstrating how this influence diminishes with distance in spatially embedded networks where nodes represent geographical areas of decreasing size as network granularity increases. The calibrated model enables identification of critical zones with disproportionate impact on spread dynamics. Network structure and spatial centrality can drive outsized regional

impacts (Barthélemy, 2011; Colak et al., 2016). Empirical studies identify bottleneck corridors and influential sub-regions (Duan et al., 2023; Zhang et al., 2019). Causal attribution methods further quantify regional contributions under disruptions (Liu et al., 2022). The following sections describe the multiscale framework through the dynamical representation of spreading processes, discuss the two use cases, and demonstrate practical applications.

2 | METHODOLOGY

2.1 | Representation of multiscale dynamics

Consider the SIR model, where each entity in the population at any given time can be in one of three states: Susceptible (S), Infected (I), or Recovered (R). The transmission rate, denoted by β , governs the transition from the



Susceptible to the Infected state, while the recovery rate, denoted by μ , governs the transition from the Infected to the Recovered state. Let S , I , and R denote the fraction of entities in each of the respective states at any given time. The dot notation (\dot{S} , \dot{I} , \dot{R}) represents the time derivative, indicating the rate at which these fractions change over time. The following are the governing equations of the SIR model:

$$\begin{aligned}\dot{S} &= -\beta SI \\ \dot{I} &= \beta SI - \mu I \\ \dot{R} &= \mu I \\ S + I + R &= 1\end{aligned}\quad (1)$$

On a network representation with N nodes, each node i in the network has its own recovery rate μ_i and a specific transmission rate to another node j denoted by β_{ij} . When transmission between a pair of nodes i and j is not feasible, as determined by the relevant adjacency matrix of the network under consideration, the corresponding transmission rate β_{ij} is assigned a value of zero. The network-based formulation extends the simple SIR model to capture the spatial structure and heterogeneity of transmission patterns across different nodes in the network.

In the network-based formulation of the SIR model, the representation of a node can vary with the level of abstraction—ranging from individual entity, such as a single street in the congestion model, to an aggregated region containing several streets. A hierarchical framework is proposed that incorporates multiple scales of representation, each with a different level of spatial granularity. This multiscale approach captures fine-scale dynamics by leveraging parametric information from coarser scales. The hierarchical modeling strategy relies on the assumption that, under a mean-field approximation, the collective behavior at a finer scale approximates the dynamics observed at a higher aggregation level. Model fits for nodes that have a higher error, based on this approximation, are visualized and discussed in Appendix F. The hierarchical scales are illustrated in Figure 1a, where scale 1 corresponds to a high-level aggregated representation of the system, while scales 2 and 3 depict increasingly detailed network structures in which multiple components are represented as nodes.

Consider the system at three different scales, where each scale consists of a network of interconnected nodes. Let n denote a node in the system using a hierarchical notation inspired by fractal-like representations, where the subscript encodes the following structural information: (i) The number of digits in the subscript indicates the scale, (ii) the first $k - 1$ digits of a node indexed by k digits identify

its parent node, and (iii) the last digit specifies the unique index at that scale (Gonzalez et al., 2001). For example, consider the node $n_{1,1,4}$: The three digits in the subscript indicate that the node belongs to scale 3; the first two digits, (1,1), identify its parent node; and the last digit, 4, serves as its unique index at this scale. Furthermore, define C_n as the set of child nodes of some given node n at the next finer scale. Now, consider scale 1 in Figure 1, where the entire system is modeled in an aggregated fashion. This representation of scale 1 introduces two parameters: β_{eff} and μ_{eff} . These parameters are termed *effective* because they encapsulate the aggregated behavior of the entire system and are subsequently used to model the system at finer scales.

To aggregate the dynamics at a given scale, the weight of node i , denoted w_i , is defined to represent the fraction of entities contained within it. Thus, w_i can represent, for example, the fraction of streets or the fraction of people contained within node i . A simplifying assumption is adopted whereby all entities are treated uniformly. For example, in the congestion model, a freeway and a local road contribute equally when computing the weight of the node they belong to. From the representation in Figure 1a, the dynamical behavior at the aggregated scale 1 is related to that at scale 2 since the nodes at scale 2 collectively constitute the node at scale 1. In this aggregation process, the contribution of each node depends on the number of entities (e.g., streets or people) it contains, which is captured in the weight w_i for node i . The following equations approximate the relationship between parameters across scales—refer to Appendix A for the derivation.

$$\beta_{\text{eff}} \approx \sum_{i,j \in C_{n_1}} w_i \beta_{ji}, \quad \mu_{\text{eff}} \approx \sum_{i \in C_{n_1}} w_i \mu_i \quad (2)$$

Equation (2) captures an approximate relationship between the model parameters at scale 1 and scale 2, see Figure 1a. Next, to relate the parameters between scales 2 and 3, the following notation is used. Let \mathcal{V}_i represent the set of all nodes at the scale i . For example, at scale 2, the set of nodes is given by $\mathcal{V}_2 = \{n_{1,1}, n_{1,2}, n_{1,3}, n_{1,4}\}$. Let i, j be two nodes at scale 2, that is, $i, j \in \mathcal{V}_2$, and let p, q be two nodes at scale 3 that are child nodes of i and j , respectively, that is, $p \in C_i$ and $q \in C_j$. Based on this notation, Equation (3) is derived under similar assumptions. This equation presents an approximate relationship between the transmission rate parameters β_{ij} and recovery rate parameter μ_i corresponding to scale 2, with the respective parameters of child nodes p, q at scale 3.

$$\beta_{ij} \approx \frac{\sum_{\substack{p \in C_i \\ q \in C_j}} w_q \beta_{pq}}{\sum_{q \in C_j} w_q}, \quad \mu_i \approx \frac{\sum_{p \in C_i} w_p \mu_p}{\sum_{p \in C_i} w_p} \quad (3)$$



Equation (3) is used to approximate the relationship between the model parameters at scale 2 and scale 3. This hierarchical modeling framework provides an approximate representation of spreading dynamics at finer scales, based on a set of simplifying assumptions. In particular, the derivation of Equation (2) and Equation (3) relies on a mean-field approximation, which assumes homogeneity within each scale and neglects higher order correlations between nodes. This approximation deteriorates in structurally heterogeneous networks, as the aggregation process across scales fails to preserve the underlying topological relationships among nodes.

The following subsection presents the methodology for applying the multiscale network framework to two spreading processes—congestion propagation on road networks and infection transmission on social contact networks—and describes the optimization procedure used for parameter estimation.

2.2 | Spatiotemporal modeling of traffic congestion and COVID-19 infection spread

To generate realistic traffic data on the road network, the open-source traffic micro-simulator, Simulation for Urban Mobility (SUMO; Lopez et al., 2018), is leveraged. The calibrated origin–destination (OD) matrices (Ambühl et al., 2023) are provided as input to the SUMO traffic simulation framework. A set of 15 traffic simulations was performed for the San Francisco Bay Area, with results averaged to yield representative traffic patterns. The simulator provides a detailed description of each of the road links in the network at 5-min time intervals. For each time step, each road link is classified as either being in a congested state or a free-flow state. This classification is based on the Fundamental Diagram of Traffic (Helbing, 2009), where the critical density of a specific road link is defined as the density at which the maximum flow occurs for that road link. A road link is classified as congested at a given time step if its observed density exceeds its critical density. Note that road links have different critical densities determined by their capacities and maximum flows. We ran the traffic simulation 15 times and modeled congestion–spread dynamics using the average across runs. Figure 2a visualizes the complete road network at 9 a.m. with congested red road links, while Figure 2b provides a zoomed-in view of the city of San Francisco at the same time. Refer to Appendix C for details on the traffic simulations for retrieving the congestion data.

Previous works (Bagabaldo et al., 2024; Saberi et al., 2020) have implemented the SIR model for modeling congestion spread, where the susceptible state corresponds to the free-flow state of road-links, the infected state cor-

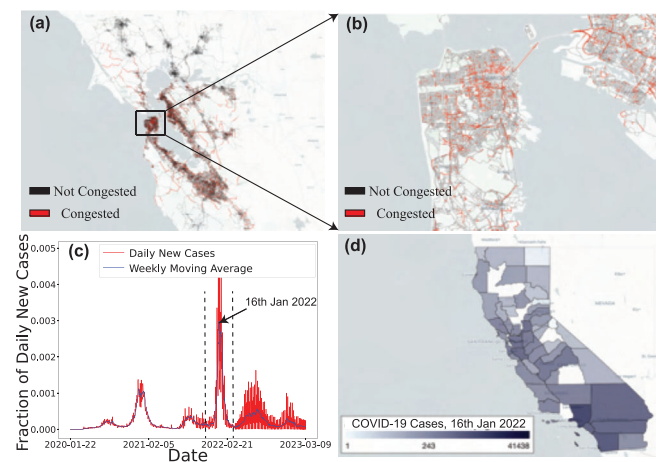


FIGURE 2 Systems of study. Traffic congestion (a,b) and COVID-19 infection (c,d) spreading. (a,b) State of the traffic congestion in the San Francisco Bay Area at 9 a.m. (c,d) Number of infections of COVID-19 per county on January 16, 2022.

responds to the congested state of road-links, while the recovered state retains its definition where a road-link has recovered from congestion. Traffic congestion during the morning commute (6–10 a.m.) is modeled by dividing the region into polygons at five scales using the Uber H3 Spatial Indexing System (H3 Geospatial Indexing System, 2018), as illustrated in Figure 1. The temporal evolution of congestion propagation, obtained from SUMO simulations, is mapped onto a multiscale network representation. At any given scale, two polygons (represented as nodes in the network, as illustrated in Figure 1b–d) are connected via the adjacency matrix if road-links cross their shared boundaries, allowing congestion to spread between them. This spatial criterion forms the basis for constructing the adjacency matrix of the network, which determines its connectivity structure. Details on the multiscale network representation for the congestion model can be found in Table B1. Details on the algorithm for the construction process are included in Appendix B.

Similarly, the COVID-19 spreading dynamics for the infection model can be represented through a multiscale SIR model. Figure 2c shows the temporal variation in the daily fraction of people infected in the state of California. The dashed lines indicate the observed peak of the Omicron variant, which is the period considered for modeling in this work, spanning from December 15, 2021, to February 14, 2022. The population of the counties in California is retrieved from the Census data (States Census Bureau, 2024). Figure 2d shows the spatial distribution of peak daily cases, grouped by county, for the day on which the highest daily new cases were recorded.

In the infection model, two spatial scales are considered, representing the state of California and its counties,



respectively. Scale 1 represents the entire state of California, while scale 2 includes 50 of the 58 counties for which data are available. The spatial granularity of the available data limits the number of scales for the infection model to 2. Furthermore, the spread of COVID-19 infection is enabled by trips made within the region of study (Pardo-Araujo et al., 2023). This is reflected in the adjacency matrix for the infection model, which is created based on the weighted directed network of trips between California's counties. These trips enable geographically distant regions to be connected in the infection model, unlike the adjacency matrix for the congestion model, which is based on direct spatial proximity. Details on the construction of the adjacency matrix for the infection model are included in Appendix D.

The SIR ordinary differential equations (ODEs) are integrated using an adaptive solver, with outputs aligned to the 5-min intervals for congestion data and daily intervals for infection data based on the fidelity of the modeled data. The corresponding model parameters for the transmission rate and recovery rate are obtained through a model fitting process. This process is framed as an optimization problem with the objective to minimize the squared error between the data and the model. First, the entire region is modeled as a single node, yielding two key parameters, β_{eff} and μ_{eff} corresponding to scale 1, as described in Equation (A1). For parameter estimation at finer scales, the model incorporates hierarchical regularization in the optimization objective, using Equation (2) when fitting scale 2, and Equation (3) when fitting scale 3 and finer. Details on the model fitting process are included in Appendix E. The objective function with the optimization problem corresponding to fitting the model at scale 2 can then be written as follows:

$$E(\theta) = \sum_{i=1}^N \sum_{t=1}^T (I_{i_t} - \hat{I}_{i_t}(\theta))^2 + \lambda_{\beta} \left(\beta_{\text{eff}} - \sum_{i=1}^N \sum_{j=1}^N w_{ij} \beta_{ji} \right)^2 + \lambda_{\mu} \left(\mu_{\text{eff}} - \sum_{i=1}^N w_i \mu_i \right)^2 + \lambda \|\theta\|^2 \quad (4)$$

Here, the first term minimizes the fitting error between the data and the model where I_{i_t} represents the fraction of infected entities in node i at time t while \hat{I}_{i_t} represents the model prediction, and θ represents the complete set of parameters. The parameters N and T represent the total number of nodes and the total time-steps for which the system has been modeled. The second term, weighted by the regularization parameter λ_{β} , encourages the transmission parameters β_{ji} to remain consistent with the approximate relationship described in Equation (2), while the third term, through λ_{μ} , similarly guides the recovery param-

eters μ_i to align with the aggregated behavior outlined in the same equation. The last term penalizes larger parametric values to reduce overfitting and limit model complexity. The regularization parameters corresponding to Equation (4) are determined based on the relative size of the error terms to penalize parameter size and implement the derived hierarchical constraints on the parameters. In the unregularized model, the parameters λ_{β} and λ_{μ} are set to 0, allowing the fit at any given scale to be agnostic to the model fit at other scales. This multiscale modeling process produces fits to the data for all considered scales, with results for the congestion model shown in Figure 3a–c and for the infection model in Figure 3d,e. The scatter points in each of these figures show the temporal variation of the fraction of infected entities, i . The effective parameters, β_{eff} and μ_{eff} correspond to scale 1 for either model, and the values are shown in the inset of Figure 3a and Figure 3d. Model fits for two of the remaining four finer scales for the congestion model are presented in Figure 3b,c while Figure 3e plots the model fit at the county level, at scale 2. This multiscale model captures variations in spreading patterns across different nodes. The following section discusses the results of this multiscale modeling framework for two different applications.

3 | RESULTS

3.1 | Validating the multiscale regularization scheme

To evaluate the effectiveness of the proposed multiscale framework, two model fitting schemes are compared. The first incorporates multiscale regularization terms that link parameters across scales and thus reflect the hierarchical nature of this framework. In the second scheme, which is unregularized, each scale is fit independently, and thus the parameters at different scales are not related. The process of fitting the model is carried out using the L-BFGS optimization algorithm, with two stopping criteria: the process terminates if the mean squared error (MSE) converges to less than 10^{-7} or if the number of optimization epochs exceeds 100,000. To mitigate the risk of convergence to local minima and to ensure robustness, each fitting procedure is repeated for 200 independent optimization runs, each initialized with randomized parameter values. Details on the model fitting process are included in Appendix E.

Figure 4a,b plot the variation in the parameters under the multiscale regularization scheme and Figure 4c,d plot the variation in the parameters under the unregularized scheme for the congestion and infection models, respectively. For visualization, a sample of 30 parameters is shown. Specifically, the first 10 parameters in each

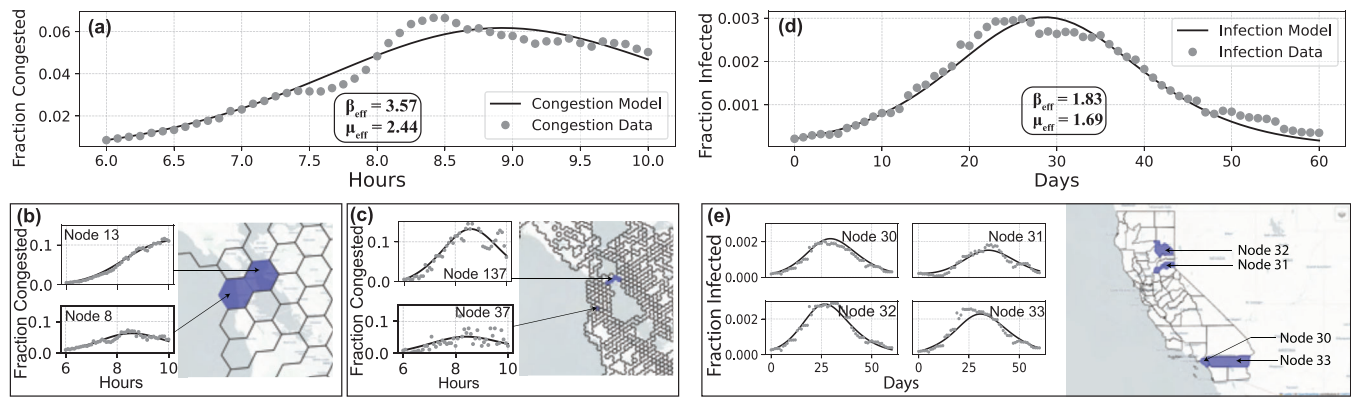


FIGURE 3 Model fits for different scales for the congestion model and the infection model. (a–c) Model fit for the whole region for the congestion model with two additional scales. (d,e) Model fit for the whole region for the infection model with one additional scale.

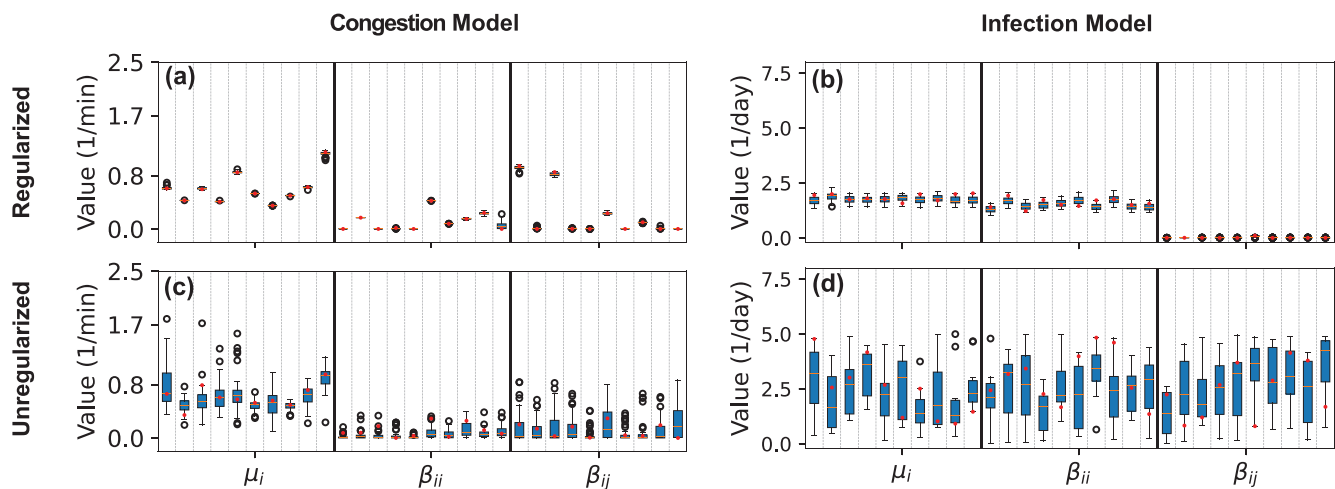


FIGURE 4 Parameter variation with and without regularization. Comparison of optimal parameter distributions ($n = 30$) for the congestion model (a,c) and infection model (b,d). Parameters estimated with regularization (a,b) show substantially lower variation compared to those estimated without regularization (c,d), demonstrating the stabilizing effect of the regularization approach.

figure correspond to the recovery rate μ_i , the next 10 correspond to the self-infection rate β_{ii} , and the final 10 correspond to the transmission rate β_{ij} . Note that the parameters for the congestion model correspond to scale 3, while those for the infection model correspond to scale 2, containing counties as nodes.

The models fit under the unregularized scheme exhibit greater variation in parameters than the model parameters fit under the regularized scheme. This difference is due to the constrained parameter search space introduced through the regularization term. With regularization, multiple iterations with varying initializations converge to the same optimal set of parameters. This pattern is consistently observed across all four successive scales of the congestion model, with the exception of scale 1, which is the coarsest scale described by the *effective* parameters. Furthermore, the MSE between the actual data and the model

predictions is consistently higher for the unregularized model, with the disparity becoming more pronounced at finer scales. This indicates that the advantages of the regularized approach are more evident when fitting multiple finer scales. Specifically, the MSE values for the unregularized and regularized models are 0.032 and 0.021 at scale 2, 0.171 and 0.142 at scale 3, and 7.40 and 1.179 at scale 4, respectively. Further discussion of the distribution of the error values for different nodes in both models is presented in Appendix F. These results are obtained under identical optimization conditions, including the same maximum number of iterations and the same convergence tolerance. Furthermore, the regularized models require less computational time to fit, as the additional regularization terms across scales reduce the parameter search space. As shown in Figure 4b, for nodes i and j , the majority of the spreading dynamics in the infection model are captured



by the self-recovery parameters μ_i and the self-infection parameters β_{ii} . In contrast, the parameters representing infection spreading rates between counties, denoted by β_{ij} , are predominantly close to zero. This suggests that COVID-19 infection spread is primarily driven by intra-county human mobility, with intercounty mobility playing a relatively minor role. The parameter variations shown in Figure 4d correspond to the infection model fit under the unregularized scheme that cannot adequately fit the real-world COVID-19 infection data due to the large number of parameters.

3.2 | Heterogeneity in spatial impacts in congestion model

This section details a specific application of the congestion model, whereby the models fit under the multiscale regularization scheme are used to quantify how congestion in neighboring regions affects a given region. At finer scales, parameters such as μ_i , β_{ii} , and β_{ij} characterize interactions between spatial regions i and j . The influence of neighboring regions is quantified by measuring the area between the original and perturbed congestion curves (Ma et al., 2022), providing a quantitative assessment of their relative impact.

The impact of a neighboring region j on the region of interest i can be mathematically represented as follows:

$$M_{ij} = \int_{t_0}^{t_1} |I_i^{(j)}(t) - I_i^{(0)}(t)| dt \quad (5)$$

$$\bar{M}_{ij} = \frac{M_{ij} - \min_{i',j'} M_{i',j'}}{\max_{i',j'} M_{i',j'} - \min_{i',j'} M_{i',j'}} \quad (6)$$

where

- (1) $I_i^{(0)}(t)$: represents the value of the congestion curve of region i at time t , under no perturbation;
- (2) $I_i^{(j)}(t)$: represents the value of the congestion curve of region i at time t , when region j is perturbed;
- (3) M_{ij} : the area between the original infection curve of region i , and the infection curve of region i when region j is perturbed;
- (4) \bar{M}_{ij} : the rescaled formulation of M_{ij} based on min-max scaling, defined as the impact of some region j on the region of interest i .

The perturbation is induced in a given region by modifying the initial condition based on which the model is simulated (Moro et al., 2021). This change can represent a traffic accident or a lane-widening event causing a sudden increase in congestion, equivalent to 10% of peak levels. The initial condition is adjusted from nearly 0 to

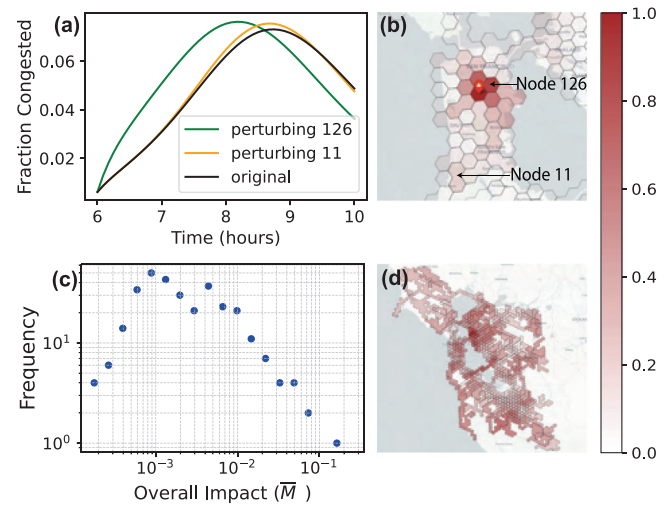


FIGURE 5 Impact matrix analysis for the congestion model. (a) Congestion curve of a sample node: baseline trajectory (black), response to perturbations at nodes 126 (green) and 94 (yellow). (b) Spatial distribution of regional impacts on the focal node (starred). (c) Log-log distribution of overall impact scores (\bar{M}_i). (d) Spatial visualization of overall impact, highlighting critical regions including Oakland City downtown and Bay bridges among others.

0.005 under the perturbed condition, based on model sensitivity. A sweep through 0%–10% changes in the initial condition showed consistent results; beyond 10% the fitted SIR model becomes sensitive, leading to significant output divergence. Perturbations of higher severity thus cannot be modeled under the current framework. When a region's congestion dynamics experience a change, the effect spreads to nearby nodes based on the transmission rate parameters β_{ij} . As a result, this perturbation leads to a different congestion curve for the surrounding regions. Specifically, the regularized model is re-evaluated using the same parameter set, but with an increased initial congestion level for the node of interest. This perturbation isolates the sensitivity of the fitted model to initial conditions, which is particularly relevant for compartmental formulations such as the SIR model. These differences in the evolution of the congestion curves are captured in the impact \bar{M}_{ij} , formulated in Equation (6). Consider a sample region, indicated with a marker in Figure 5b, along with two nearby regions indexed as 11 and 126. Figure 5a illustrates the congestion curves for the given region under no perturbation, and when specific surrounding regions are perturbed, also highlighting the area between the original and perturbed curves for the two perturbations scenarios. Additionally, Figure 5b depicts the degree of impact that surrounding regions exert on the region of interest, located within the metropolitan region of San Francisco. This analysis provides a framework for identifying critical parts of the network that influence the congestion dynamics corresponding to the region under consideration.

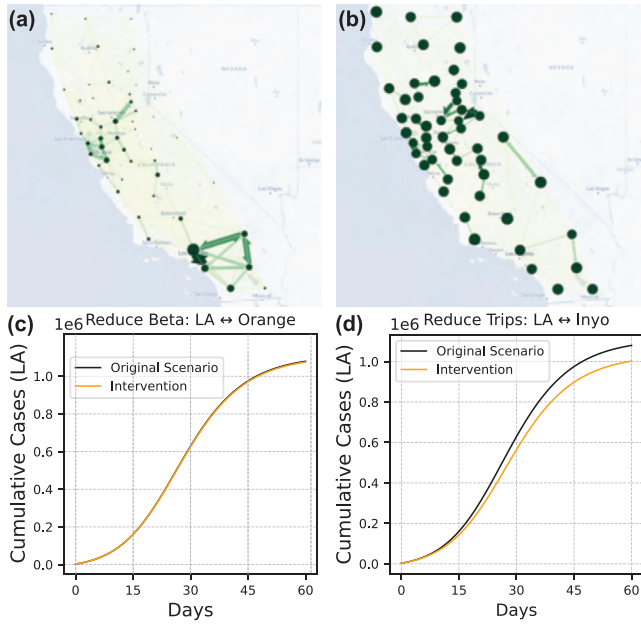


FIGURE 6 Impact of targeted intervention on infection dynamics. (a) Visualization of the intercounty trips in California. (b) Spatial visualization of the transmission rate, β , matrix. (c) Infection curves under intervention based purely on trip counts. Note that there is minimal decrease in the projected cases. (d) Infection curves under intervention based on the trip counts in addition to the transmission rate, β , parameters from the regularized model. Note the substantive difference decrease in the projected cases.

Moreover, the impact analysis can be extended to measure the overall influence of a specific region on the entire system. Instead of analyzing only pairwise effects between regions, this approach assesses how a perturbation in one region's congestion state influences all other regions across time. The overall impact is defined as the average area between the perturbed and unperturbed curves across all regions (excluding the perturbed one), normalized using min-max scaling as follows.

$$M_i = \frac{1}{N-1} \sum_{\substack{j=1 \\ j \neq i}}^N M_{ij} \quad (7)$$

$$\bar{M}_i = \frac{M_i - \min_{i'} M_{i'}}{\max_{i'} M_{i'} - \min_{i'} M_{i'}} \quad (8)$$

where:

- (1) $I_i^{(0)}(t)$: represents the value of the congestion curve of region a at time t , under no perturbation;
- (2) $I_i^{(j)}(t)$: represents the value of the congestion curve of region i at time t , when region j is perturbed;
- (3) M_i : the overall impact of region i on the system, defined as the sum of the area between the original infection curve of region i , and the infection curve of

region j when region j is perturbed, summed up over all possible regions j ;

- (4) \bar{M}_i : the rescaled formulation of M_{ij} through min-max scaling, defined as the overall impact of region i on the complete system.

The overall impact, \bar{M}_i , then measures the influence of the given region i on all of the other regions in the system, identifying critical regions that significantly contribute to the congestion spreading dynamics. Figure 5c illustrates the distribution of \bar{M}_i across all the regions. While most spatial regions exhibit nominal overall impact, a few at the tail end make disproportionately large contributions. It should also be noted that a relatively fewer number of regions have a very low extent of impact. A visualization of the spatial distribution of \bar{M}_i is shown in Figure 5d. Notably, the regions associated with a key bridge in the San Francisco Bay Area exhibit exceptionally high impact on system-wide congestion dynamics, as do the cities of San Francisco to the west and Oakland to the east.

3.3 | Targeted intervention through trips matrix in infection model

For the infection model in the state of California at the county level, modeling efforts are constrained by the limited availability of infection data, which typically consist only of the temporal evolution of reported cases. Within this context, the trips matrix serves as a crucial tool for understanding and quantifying mobility-driven transmission dynamics. By analyzing the travel patterns at the county level, key pathways of infection spread can be identified, enabling the design of targeted mobility interventions to effectively mitigate disease propagation (Moreno López et al., 2025; Pardo-Araujo et al., 2023). See Appendix D for a discussion of the probability density distribution of the trips with distance.

To ensure that the transmission rate parameter β_{ij} reflects the infection spread per outbound trip from county i to county j , the trip matrix (shown in Figure 6a) is normalized by the total number of trips originating from the county, before being incorporated into the model as the adjacency matrix. See the Methods section for details on the creation of the outflow-normalized adjacency matrix. Enabled through the model fit under the regularized scheme, Figure 6b presents a spatial visualization of the transmission rate parameters β_{ij} for the infection model, with each node representing a county in California similar to Figure 6a. In this case, the size of each node reflects the self-infection parameter β_{ii} , while the directed edges and their width correspond to the off-diagonal entries in the β matrix, the entries of which are represented by β_{ij} . The visualization reveals that the majority of the infection



dynamics are captured by the self-infection parameters β_{ii} , whereas the interaction parameters β_{ij} are nearly negligible. This suggests that most infections arise from self-trips occurring within the same county, with relatively less propagation of infection between counties.

To effectively contain the spread of infection facilitated by human mobility, the regularized model captures the transmission rate associated with travelers moving from county i to county j , represented by β_{ij} , while also considering the total number of trips between these counties. This approach is grounded in the proposed multiscale regularization scheme through which the model parameters are obtained, which allows for a nuanced understanding of infection dynamics. Consider the Los Angeles County in California. To contain the spread of infection by restricting human mobility, a naive approach is to limit the trips between Los Angeles and the county with the highest volume of travel between them, which in this case is Orange County. Despite a substantial reduction of 50% in trips between this pair of counties, amounting to 11 million trips, the curves depicting the temporal variation of cumulative cases in Los Angeles County under this intervention (DeVerna et al., 2025; Guo et al., 2015; Vedam & Ghose, 2023), as shown in Figure 6c, remain nearly indistinguishable. However, this approach overlooks the critical factor of infection transmission rates per outbound traveler, represented by β_{ij} .

Instead, the targeted intervention strategy based on the regularized model recommends reducing trips between Los Angeles and the county pair with the highest product of the transmission rate β_{ij} and the number of trips. This ensures that both the volume of travel and the infection transmission potential are accounted for, since the goal is to reduce the spread of infection and not just limit certain trips (Wallinga et al., 2009). Applying this strategy identifies Los Angeles and Inyo County as one of the most impactful pair for trip reduction. By reducing the number of trips between these pair of counties by 50%, which corresponds to reducing approximately 15,000 trips, the regularized model predicts a consequent decrease of 60,000 cumulative cases in Los Angeles County, as shown in Figure 6d. Such a targeted intervention, guided by the specific parameters β_{ij} which are stored in the β matrix, effectively leverages the model's detailed representation of infection transmission dynamics across the network, and thus offers a more efficient approach to controlling the spread of infection.

4 | CONCLUSION

This study introduced a multiscale hierarchical framework for modeling spreading dynamics on complex

networks using the compartmental SIR model. The approach integrates parameter relationships across scales via a mean-field approximation-based regularization scheme, enabling consistent and computationally efficient inference of spreading parameters at varying levels of granularity.

The framework was validated through two distinct applications: traffic congestion propagation across road networks and infection transmission across social contact networks. In both cases, hierarchical regularization improved model stability and convergence compared to the baseline SIR formulation, reducing computation time by 66% for fitting the finest scale of the congestion model, and reducing average model error by over sixfolds at the finest scale.

At finer spatial scales, the model quantified interregional influences through node-specific transmission and recovery parameters. In the congestion model, a small subset of nodes contributed over two orders of magnitude more to the overall impact on the system. In the infection model, despite coarser data resolution, fitted parameters enabled the identification of critical travel connections, which when restricted by 15,000 trips reduced cumulative infection levels in Los Angeles County by 6%.

Overall, the hierarchical structure of the framework enables consistent analysis of spreading phenomena across multiple scales while preserving essential system-level dynamics. Nonetheless, the current weighting scheme assumes no heterogeneity within entities, which can mask variation in exposure, and reporting in the infection model, and different road capacities in the congestion model. The modeling horizon, grounded in an SIR formulation, captures only a single peak and thus cannot represent multi-wave or strongly nonstationary dynamics without extensions. In the congestion application, heterogeneity in internode connections (e.g., capacities, directionality) is not encoded by the weights and may bias inferred influences. We also observe that higher weight nodes tend to have lower model error; while Algorithm 1 provides a polygon-merging procedure to increase weights and attenuate measurement noise, more sophisticated aggregation and denoising strategies are left for future work.

CONFLICT OF INTEREST STATEMENT

The authors declare no potential conflicts of interest.

REFERENCES

- Ambühl, L., Menendez, M., & González, M. C. (2023). Understanding congestion propagation by combining percolation theory with the macroscopic fundamental diagram. *Communications Physics*, 6(1), 1–7.
- Bagabaldo, A. R., Gan, Q., Bayen, A. M., & González, M. C. (2024). Impact of navigation apps on congestion and spread dynamics on



- a transportation network. *Data Science for Transportation*, 6(2), 1–13.
- Balcan, D., Colizza, V., Gonçalves, B., Hu, H., Ramasco, J. J., & Vespignani, A. (2009). Multiscale mobility networks and the spatial spreading of infectious diseases. *Proceedings of the National Academy of Sciences*, 106(51), 21484–21489.
- Barthélemy, M. (2011). Spatial networks. *Physics Reports*, 499(1–3), 1–101.
- Bettencourt, L. M., Cintrón-Arias, A., Kaiser, D. I., & Castillo-Chávez, C. (2006). The power of a good idea: Quantitative modeling of the spread of ideas from epidemiological models. *Physica A: Statistical Mechanics and its Applications*, 364, 513–536.
- Boeing, G., & Ha, J. (2024). Resilient by design: Simulating street network disruptions across every urban area in the world. *Transportation Research Part A: Policy and Practice*, 182, 104016.
- Chang, S., Pierson, E., Koh, P. W., Gerardin, J., Redbird, B., Grusky, D., & Leskovec, J. (2020). Mobility network models of Covid-19 explain inequities and inform reopening. *Nature*, 589(7840), 82–87.
- Chen, Y., Shafi, S. Y., & Chen, Y.-f. (2020). Simulation pipeline for traffic evacuation in urban areas and emergency traffic management policy improvements through case studies. *Transportation Research Interdisciplinary Perspectives*, 7, 100210.
- Colak, S., Lima, A., & González, M. C. (2016). Understanding congested travel in urban areas. *Nature Communications*, 7(1), 1–8.
- Colizza, V., Pastor-Satorras, R., & Vespignani, A. (2007). Reaction–diffusion processes and metapopulation models in heterogeneous networks. *Nature Physics*, 3(4), 276–282.
- Cornacchia, G., Lemma, L., & Pappalardo, L. (2024). Alternative routing based on road popularity. General chairs, ACM SIGSPATIAL 2024: In M. Nascimento, L. Xiong, A. Zufle (Eds.), *Proceedings of the 2nd ACM SIGSPATIAL workshop on sustainable urban mobility* (pp. 14–17). ACM.
- Das, S., Samaei, M. H., & Scoglio, C. (2024). SIR epidemics in interconnected networks: Threshold curve and phase transition. *Applied Network Science*, 9(1), 1–24.
- De Domenico, M., Granell, C., Porter, M. A., & Arenas, A. (2016). The physics of spreading processes in multilayer networks. *Nature Physics*, 12(10), 901–906.
- DeVerna, M. R., Pierri, F., Ahn, Y.-Y., Fortunato, S., Flammini, A., & Menczer, F. (2025). Modeling the amplification of epidemic spread by individuals exposed to misinformation on social media. *npj Complexity*, 2(1), 1–8.
- Ding, C., Song, Y., Zhang, H., & Wang, T. (2025). Uncertainty quantification in Bayesian physics-informed deep learning-based traffic state prediction. *Computer-Aided Civil and Infrastructure Engineering*, 40, 4845–4864.
- Duan, J., Zeng, G., Serok, N., Li, D., Lieberthal, E. B., Huang, H.-J., & Havlin, S. (2023). Spatiotemporal dynamics of traffic bottlenecks yields an early signal of heavy congestions. *Nature Communications*, 14(1), 1–11.
- Gallotti, R., Maniscalco, D., Barthélemy, M., & De Domenico, M. (2024). Distorted insights from human mobility data. *Communications Physics*, 7(1), 1–10.
- Ganin, A. A., Kitsak, M., Marchese, D., Keisler, J. M., Seager, T., & Linkov, I. (2017). Resilience and efficiency in transportation networks. *Science Advances*, 3(12), 1–8.
- Gao, J. (2024). Intrinsic simplicity of complex systems. *Nature Physics*, 20(2), 184–185.
- Gao, J., Barzel, B., & Barabási, A.-L. (2016). Universal resilience patterns in complex networks. *Nature*, 530(7590), 307–312.
- Gonzalez, M., Araujo, M., & Rodriguez, A. (2001). Flow equations on a fractal structure. *Physica A: Statistical Mechanics and Its Applications*, 298(3–4), 297–314.
- González, M. C., & Barabási, A.-L. (2007). From data to models. *Nature Physics*, 3(4), 224–225.
- Guo, D., Li, K. C., Peters, T. R., Snively, B. M., Poehling, K. A., & Zhou, X. (2015). Multi-scale modeling for the transmission of influenza and the evaluation of interventions toward it. *Scientific Reports*, 5(1), 1–9.
- H3 Geospatial Indexing System. (2018). *H3 geospatial indexing system PLBIBITALIC—h3geo.org*. <https://h3geo.org>
- Helbing, D. (2009). Derivation of a fundamental diagram for urban traffic flow. *The European Physical Journal B*, 70(2), 229–241.
- Jiang, X., & Adeli, H. (2004). Object-oriented model for freeway work zone capacity and queue delay estimation. *Computer-Aided Civil and Infrastructure Engineering*, 19(2), 144–156. <https://doi.org/10.1111/j.1467-8667.2004.00344.x>
- Keeling, M. J., & Rohani, P. (2008). *Modeling infectious diseases in humans and animals*. Princeton University Press.
- Kozhabek, A., Chai, W. K., & Zheng, G. (2024). Modeling traffic congestion spreading using a topology-based SIR epidemic model. *IEEE Access*, 12, 35813–35826.
- Lengyel, B., Bokányi, E., Di Clemente, R., Kertész, J., & González, M. C. (2020). The role of geography in the complex diffusion of innovations. *Scientific Reports*, 10(1), 15065.
- Li, Y., Zhao, L., Yu, Z., & Wang, S. (2017). Traffic flow prediction with big data: A learning approach based on SIS-complex networks. In *2017 IEEE 2nd information technology, networking, electronic and automation control conference (ITNEC)* (pp. 550–554). IEEE, https://www.aconf.org/conf_99336.html
- Liu, X., Li, D., Ma, M., Szymanski, B. K., Stanley, H. E., & Gao, J. (2022). Network resilience. *Physics Reports*, 971, 1–108.
- Lopez, P. A., Wiessner, E., Behrisch, M., Bieker-Walz, L., Erdmann, J., Flotterod, Y.-P., Hilbrich, R., Lucken, L., Rummel, J., & Wagner, P. (2018). Microscopic traffic simulation using sumo. In *2018 21st international conference on intelligent transportation systems (ITSC)* (pp. 2575–2582). IEEE.
- Ma, C., Li, X., Zhao, Z., Liu, F., Zhang, K., Wu, A., & Nie, X. (2022). Understanding dynamics of pandemic models to support predictions of Covid-19 transmission: Parameter sensitivity analysis of SIR-type models. *IEEE Journal of Biomedical and Health Informatics*, 26(6), 2458–2468.
- Moreno López, J. A., Mateo, D., Hernando, A., Meloni, S., & Ramasco, J. J. (2025). Critical mobility in policy making for epidemic containment. *Scientific Reports*, 15(1), 1–13.
- Moro, E., Frank, M. R., Pentland, A., Rutherford, A., Cebrian, M., & Rahwan, I. (2021). Universal resilience patterns in labor markets. *Nature Communications*, 12(1), 1–8.
- Ogilvy Kermack, W., & McKendrick, A. (1927). A contribution to the mathematical theory of epidemics. *Proceedings of the Royal Society of London. Series A, Containing Papers of a Mathematical and Physical Character*, 115(772), 700–721.
- Olmos, L. E., Çolak, S., Shafiei, S., Saberi, M., & González, M. C. (2018). Macroscopic dynamics and the collapse of urban traffic. *Proceedings of the National Academy of Sciences*, 115(50), 12654–12661.
- Overton, C. E., Wilkinson, R. R., Loyinmi, A., Miller, J. C., & Sharkey, K. J. (2021). Approximating quasi-stationary behaviour



- in network-based sis dynamics. *Bulletin of Mathematical Biology*, 84(1), 1–32.
- Pardo-Araujo, M., García-García, D., Alonso, D., & Bartumeus, F. (2023). Epidemic thresholds and human mobility. *Scientific Reports*, 13(1), 1–15.
- Pastor-Satorras, R., & Vespignani, A. (2001). Epidemic spreading in scale-free networks. *Physical Review Letters*, 86(14), 3200–3203.
- Replica. (2024). *Replica, data to drive decisions about the built environment*. <https://www.replicahq.com>
- Rodrigues, H. S. (2016). Application of SIR epidemiological model: New trends. *International Journal of Applied Mathematics and Informatics*, 10, 92–97.
- Saberi, M., Hamedmoghadam, H., Ashfaq, M., Hosseini, S. A., Gu, Z., Shafiei, S., Nair, D. J., Dixit, V., Gardner, L., Waller, S. T., & González, M. C. (2020). A simple contagion process describes spreading of traffic jams in urban networks. *Nature Communications*, 11(1), 1–9.
- Salgado, A., He, Y., Radke, J., Ganguly, A. R., & Gonzalez, M. C. (2024). Dimension reduction approach for understanding resource-flow resilience to climate change. *Communications Physics*, 7(1), 1–12.
- Smith, D., Djahel, S., & Murphy, J. (2014). A SUMO based evaluation of road incidents' impact on traffic congestion level in smart cities. In *39th annual IEEE conference on local computer networks workshops* (pp. 702–710). IEEE.
- States Census Bureau, U. (2024). *United States Census Bureau*. <https://www2.census.gov/programs-surveys/popest/datasets/2020-2023/counties/totals/co-est2023-alldata.csv>
- Stolerman, L. M., Coombs, D., & Boatto, S. (2015). SIR-network model and its application to dengue fever. *SIAM Journal on Applied Mathematics*, 75(6), 2581–2609.
- Thibeault, V., Allard, A., & Desrosiers, P. (2024). The low-rank hypothesis of complex systems. *Nature Physics*, 20(2), 294–302.
- Toole, J. L., Cha, M., & González, M. C. (2012). Modeling the adoption of innovations in the presence of geographic and media influences. *PLoS One*, 7(1), e29528.
- Tu, C., D'Odorico, P., & Suweis, S. (2021). Dimensionality reduction of complex dynamical systems. *iScience*, 24(1), 101912.
- Vedam, N., & Ghose, D. (2023). The impact of mobility and interventions on the spread of diseases. *IEEE Transactions on Computational Social Systems*, 10(5), 2291–2311.
- Wallinga, J., van Boven, M., & Lipsitch, M. (2009). Optimizing infectious disease interventions during an emerging epidemic. *Proceedings of the National Academy of Sciences*, 107(2), 923–928.
- Wikle, C. K. (2003). Hierarchical Bayesian models for predicting the spread of ecological processes. *Ecology*, 84(6), 1382–1394.
- Zhang, L., Zeng, G., Li, D., Huang, H.-J., Stanley, H. E., & Havlin, S. (2019). Scale-free resilience of real traffic jams. *Proceedings of the National Academy of Sciences*, 116(18), 8673–8678.
- Zhang, T., Wang, J., Wang, T., Pang, Y., Wang, P., & Wang, W. (2023). A deep marked graph process model for citywide traffic congestion forecasting. *Computer-Aided Civil and Infrastructure Engineering*, 39(8), 1180–1196.
- Zhang, Y., Li, S., Zhang, J., Ma, J., & An, H. (2022). Traffic-driven SI epidemic spreading on scale-free networks. *International Journal of Modern Physics C*, 33(08).
- Zhao, L., Zou, L., Wang, Z., Song, T., Schonfeld, P., Chen, F., Li, R., & Li, P. (2025). Multi-task graph-based model for metro flow prediction under dynamic urban conditions. *Computer-Aided Civil and Infrastructure Engineering*, 40(21), 3239–3258.

How to cite this article: Kasliwal, A., Alhadlaq, A., Salgado, A., Ganguly, A. R., & González, M. C. (2025). Hierarchical analysis of spreading dynamics in complex systems. *Computer-Aided Civil and Infrastructure Engineering*, 40, 6223–6241. <https://doi.org/10.1111/mice.70165>

APPENDIX A: SIR MODEL FRAMEWORK FOR HIERARCHICAL MULTISCALE NETWORKS

Consider a multiscale network comprising three representative spatial scales—1, 2, and 3—arranged in order of increasing granularity, as shown in Figure A1. For clarity, edges at a given scale (i.e., connections between nodes within the same scale) are omitted from the visualization. The edges that cross the dashed lines represent hierarchical relationships between nodes at adjacent scales.

These representative scales and respective nodes within them can be described as follows:

- (1) Scale 1 contains node n_1 . The total weight of this node is $w_{n_1} = 1$, since this node includes all entities contained in this network, by definition.
- (2) Scale 2 contains nodes $n_{1,1}$, $n_{1,2}$, and $n_{1,3}$. At scale 2, the total weight w_{n_1} is distributed among these three nodes, and thus $\sum_{i=1}^3 w_{n_{1,i}} = w_{n_1} = 1$.
- (3) Scale 3 contains nodes $n_{1,1,1}$, ..., $n_{1,3,3}$. Each node has an associated weight (e.g., the weight of node $n_{1,2,1}$,

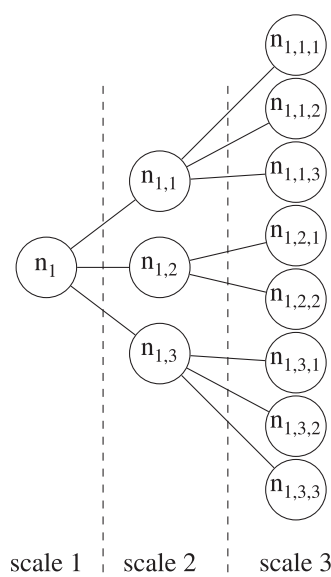


FIGURE A1 Abstract visualization of three different scales. Connections between scales represent the parent in the coarser scale. Note that the edge links that connect the nodes at any given scale are not shown for the sake of simplicity.



denoted $w_{n_{1,2,1}}$, representing the fraction of entities it contains—where an entity responds to a road link in the congestion model and to an individual in the infection model. Furthermore, the weights between nodes of scales 2 and 3 can be related as follows:

$$\sum_{i=1}^3 w_{n_{1,1,i}} = w_{n_{1,1}}$$

Proportions of the population in the Susceptible, Infected, and Recovered compartments are represented by S , I , and R , respectively (Das et al., 2024; Keeling & Rohani, 2008; Overton et al., 2021), with “dot” notation indicating derivatives with respect to time. Refer to Equation (1) for the equations of the SIR model.

By substituting the value of S , the system of Equations (1) can be written compactly as:

$$\begin{aligned} \dot{I} &= (1 - I - R)\beta I - \mu I \\ \dot{R} &= \mu I \end{aligned} \quad (\text{A1})$$

The equations above describe the SIR model in the case where the entire system is represented by a single node, meaning that this node encapsulates the aggregate behavior of the whole system. The framework is extended to multiscale networks, as illustrated in Figure A1, enabling modeling at finer scales.

First, notation is introduced to represent sets of nodes at each scale and their hierarchical relationships. Let \mathcal{V}_1 , \mathcal{V}_2 , and \mathcal{V}_3 denote nodes at scales 1, 2, and 3, respectively, and let C_n denote the set of child nodes for any node n at the next finer scale. This hierarchy enables consistent and mathematically tractable modeling of infection dynamics across scales. Fractal-like indexing for the multiscale network is used as described in Section 2.1, which allows the fraction of infected entities, I , to be related across scales.

$$I_{n_1} = \sum_{i \in \mathcal{V}_2} w_i \cdot I_i = \sum_{j \in \mathcal{V}_3} w_j \cdot I_j \quad (\text{A2})$$

$$I_{n_{1,1}} = \frac{1}{w_{n_{1,1}}} \sum_{j \in C_{n_{1,1}}} w_j \cdot I_j \quad (\text{A3})$$

$$w_{n_{1,1}} = \sum_{j \in C_{n_{1,1}}} w_j \quad (\text{A4})$$

Equations (A2)–(A4) illustrate how the infection dynamics at different levels of the hierarchy are interconnected. Specifically, Equation (A2) expresses the dynamics at node n_1 as a weighted aggregation of the dynamics of all nodes at scale 2, or equivalently, as an aggregation over all nodes at scale 3. Note that $i \in \mathcal{V}_2$ represents that i belongs to the set \mathcal{V}_2 . Equation (A3) then describes the dynamics of a specific node at scale 2, namely $n_{1,1}$, as a weighted sum of the dynamics of its children in the

set $C_{n_{1,1}}$. Finally, Equation (A4) formalizes the relation between node weights across scales, expressing the weight of node $n_{1,1}$ at scale 2 as the sum of the weights of all its children at scale 3.

This multiscale structure is applied to the SIR model to describe epidemic dynamics across spatially distributed systems. In this framework, each node n typically corresponds to a geographically distinct region, allowing the model to capture disease spread across multiple spatial scales.

Following the compact notation from Equation (A1), the equations for the SIR model on a network can be written in the following way.

$$\begin{aligned} \dot{I}_i &= (1 - I_i - R_i) \sum_{j=1}^N \beta_{ji} I_j - \mu_i I_i, \quad \text{where } i, j \in \{1, 2, \dots, N\} \\ \dot{R}_i &= \mu_i I_i \end{aligned} \quad (\text{A5})$$

Note that β_{ji} represents the transmission rate from node j to node i , and the summation over the index j captures the cumulative influence from all nodes that can transmit to node i . In such a network case, the infection spreads directly from a given node to other nodes that are connected to it—as governed by the connectivity structure of the network.

Consider scales 1 and 2, where node n_1 at scale 1 represents an aggregation of all nodes at scale 2, that is, $C_{n_1} = \mathcal{V}_2 = \{n_{1,1}, n_{1,2}, n_{1,3}\}$, as shown in Figure A1. The effective fraction of infected entities associated with node n_1 is then given by:

$$I_{n_1} = I_{\text{eff}} \approx \sum_{i \in C_{n_1}} w_i I_i \quad (\text{A6})$$

where w_i denotes the fraction of total entities residing in node i , satisfying $\sum_{i \in C_{n_1}} w_i = 1$.

Expressions for the effective transmission and recovery rates, β_{eff} and μ_{eff} , are derived by differentiating Equation (A6) with respect to time:

$$\dot{I}_{\text{eff}} = \sum_{i \in C_{n_1}} w_i \dot{I}_i \quad (\text{A7})$$

Substituting the node-level dynamics from Equation (A5) into the right-hand side yields:

$$\dot{I}_{\text{eff}} = \sum_{i \in C_{n_1}} w_i \left[(1 - I_i - R_i) \sum_{j \in C_{n_1}} \beta_{ji} I_j - \mu_i I_i \right] \quad (\text{A8})$$



Separating the two terms gives:

$$\dot{I}_{\text{eff}} = \underbrace{\sum_{i \in C_{n_1}} w_i (1 - I_i - R_i)}_{\mathcal{T}_1} \underbrace{\sum_{j \in C_{n_1}} \beta_{ji} I_j}_{\mathcal{T}_2} - \sum_{i \in C_{n_1}} w_i \mu_i I_i \quad (\text{A9})$$

To approximate \mathcal{T}_1 , the mean-field approximation is invoked to decouple the product of the terms under the assumption that the terms $(1 - I_i - R_i)$ and $\sum_{j \in C_{n_1}} \beta_{ji} I_j$ are weakly correlated:

$$\mathcal{T}_1 \approx \left(1 - \sum_{i \in C_{n_1}} w_i I_i - \sum_{i \in C_{n_1}} w_i R_i \right) \left(\sum_{i \in C_{n_1}} w_i \sum_{j \in C_{n_1}} \beta_{ji} I_j \right) \quad (\text{A10})$$

Using the definitions of the effective infected and recovered populations:

$$I_{\text{eff}} = \sum_{i \in C_{n_1}} w_i I_i, \quad R_{\text{eff}} = \sum_{i \in C_{n_1}} w_i R_i$$

this simplifies to:

$$\mathcal{T}_1 \approx (1 - I_{\text{eff}} - R_{\text{eff}}) \left(\sum_{i \in C_{n_1}} w_i \sum_{j \in C_{n_1}} \beta_{ji} I_j \right) \quad (\text{A11})$$

For notational compactness, define:

$$G_i = \sum_{j \in C_{n_1}} \beta_{ji}, \quad g_{ji} = \frac{\beta_{ji}}{G_i}$$

where G_i is the total incoming transmission rate to node i , and g_{ji} is the normalized influence of node j on i , such that $\sum_{j \in C_{n_1}} g_{ji} = 1$. Then,

$$\mathcal{T}_1 \approx (1 - I_{\text{eff}} - R_{\text{eff}}) \sum_{i, j \in C_{n_1}} w_i G_i g_{ji} I_j \quad (\text{A12})$$

The following approximation is applied:

$$\sum_{i, j \in C_{n_1}} g_{ji} w_i \approx w_j$$

which reflects the heuristic that nodes with higher weight exert greater influence. This approximation has a 12% relative error for the finest scale of the congestion model. This yields:

$$\mathcal{T}_1 \approx (1 - I_{\text{eff}} - R_{\text{eff}}) \left(\sum_{i \in C_{n_1}} w_i G_i \right) \left(\sum_{j \in C_{n_1}} w_j I_j \right) \quad (\text{A13})$$

Recognizing $I_{\text{eff}} = \sum_{j \in C_{n_1}} w_j I_j$, and defining:

$$\beta_{\text{eff}} = \sum_{i \in C_{n_1}} w_i G_i = \sum_{i, j \in C_{n_1}} w_i \beta_{ji} \quad (\text{A14})$$

This finally yields:

$$\mathcal{T}_1 \approx (1 - I_{\text{eff}} - R_{\text{eff}}) \beta_{\text{eff}} I_{\text{eff}} \quad (\text{A15})$$

Now consider the second term, \mathcal{T}_2 . Under the assumption that μ_i and I_i are uncorrelated, this term can be approximated as follows:

$$\mathcal{T}_2 \approx \left(\sum_{i \in C_{n_1}} w_i \mu_i \right) \left(\sum_{i \in C_{n_1}} w_i I_i \right) \quad (\text{A16})$$

Defining:

$$\mu_{\text{eff}} = \sum_{i \in C_{n_1}} w_i \mu_i \quad (\text{A17})$$

Using Equation (A6), the following is obtained:

$$\mathcal{T}_2 \approx \mu_{\text{eff}} I_{\text{eff}} \quad (\text{A18})$$

Substituting Equations (A15) and (A18) into Equation (A9), the effective dynamics become:

$$\dot{I}_{\text{eff}} \approx (1 - I_{\text{eff}} - R_{\text{eff}}) \beta_{\text{eff}} I_{\text{eff}} - \mu_{\text{eff}} I_{\text{eff}} \quad (\text{A19})$$

where:

$$\beta_{\text{eff}} \approx \sum_{i, j \in C_{n_1}} w_i \beta_{ji}, \quad \mu_{\text{eff}} \approx \sum_{i \in C_{n_1}} w_i \mu_i \quad (\text{A20})$$

This completes the derivation of the effective parameters across the two scales, in the special case where the coarser node n_1 aggregates the full fine-grained system, which was presented in Equation (2).

Next, consider scales 2 and 3. In this case, multiple nodes at scale 2 (e.g., $n_{1,1}$, $n_{1,2}$) aggregate their respective child nodes from scale 3. For any node i at scale 2, the relationship between the aggregated variable I_i and the individual node variables I_p for a node $p \in C_i$ at scale 3 can be expressed as:

$$I_i \approx \frac{\sum_{p \in C_i} w_p I_p}{\sum_{p \in C_i} w_p} \quad (\text{A21})$$

Following a similar procedure, differentiating the above equation with respect to time and substituting \dot{I}_p from Equation (A5) gives:

$$\dot{I}_i = \frac{1}{\sum_{p \in C_i} w_p} \cdot \sum_{p \in C_i} w_p \left[(1 - I_p - R_p) \sum_{q \in \mathcal{V}_3} \beta_{qp} I_q - \mu_p I_p \right] \quad (\text{A22})$$



Separating the two terms gives:

$$\dot{I}_i = \underbrace{\frac{1}{\sum_{p \in C_i} w_p} \sum_{p \in C_i} w_p (1 - I_p - R_p) \sum_{q \in \mathcal{V}_3} \beta_{qp} I_q}_{\mathcal{T}_1} - \underbrace{\frac{1}{\sum_{p \in C_i} w_p} \sum_{p \in C_i} w_p \mu_p I_p}_{\mathcal{T}_2} \quad (\text{A23})$$

To approximate \mathcal{T}_1 , the mean-field approximation is invoked to decouple the product of the terms under the assumption that the terms $(1 - I_p - R_p)$ and $\sum_{q \in \mathcal{V}_3} \beta_{qp} I_q$ are weakly correlated:

$$\mathcal{T}_1 \approx \frac{1}{\sum_{p \in C_i} w_p} \left(\sum_{p \in C_i} w_p - \sum_{p \in C_i} w_p I_p - \sum_{p \in C_i} w_p R_p \right) \times \left(\sum_{p \in C_i} w_p \sum_{q \in \mathcal{V}_3} \beta_{qp} I_q \right) \quad (\text{A24})$$

Using the definitions of the effective infected and recovered populations for the node i from Equation (A21) gives:

$$\mathcal{T}_1 \approx (1 - I_i - R_i) \left(\sum_{p \in C_i} w_p \sum_{q \in \mathcal{V}_3} \beta_{qp} I_q \right) \quad (\text{A25})$$

This can be rewritten as:

$$\mathcal{T}_1 \approx (1 - I_i - R_i) \sum_{q \in \mathcal{V}_3} \left(\sum_{p \in C_i} w_p \beta_{qp} \right) I_q \quad (\text{A26})$$

Expressing this in terms of the aggregated variables at scale 2, and noting that $\mathcal{V}_3 = \bigcup_{j \in \mathcal{V}_2} C_j$, the summation over $q \in \mathcal{V}_3$ becomes:

$$\mathcal{T}_1 \approx (1 - I_i - R_i) \sum_{j \in \mathcal{V}_2} \sum_{q \in C_j} \left(\sum_{p \in C_i} w_p \beta_{qp} \right) I_q \quad (\text{A27})$$

The individual node variables I_q are expressed in terms of the aggregated variables I_j . From Equation (A21), it follows that:

$$I_j = \frac{\sum_{q \in C_j} w_q I_q}{\sum_{q \in C_j} w_q} \quad (\text{A28})$$

This implies:

$$\sum_{q \in C_j} w_q I_q = \left(\sum_{q \in C_j} w_q \right) I_j \quad (\text{A29})$$

Substituting this back into the expression for \mathcal{T}_1 :

$$\mathcal{T}_1 \approx (1 - I_i - R_i) \sum_{j \in \mathcal{V}_2} \left(\sum_{p \in C_i} \sum_{q \in C_j} w_p \beta_{qp} \right) I_j \quad (\text{A30})$$

The effective transmission rate from node i to node j at scale 2 is defined as:

$$\beta_{ij} = \frac{\sum_{p \in C_i} \sum_{q \in C_j} w_p \beta_{qp}}{\sum_{p \in C_i} w_p} \quad (\text{A31})$$

This gives:

$$\mathcal{T}_1 \approx (1 - I_i - R_i) \sum_{j \in \mathcal{V}_2} \beta_{ij} I_j \quad (\text{A32})$$

Consider the second term, \mathcal{T}_2 . Under the assumption that the terms μ_p and I_p are uncorrelated, this term can be approximated as follows:

$$\mathcal{T}_2 \approx \frac{1}{\sum_{p \in C_i} w_p} \cdot \left(\sum_{p \in C_i} w_p \mu_p \right) \left(\sum_{p \in C_i} w_p I_p \right) \quad (\text{A33})$$

Defining:

$$\mu_i = \frac{\sum_{p \in C_i} w_p \mu_p}{\sum_{p \in C_i} w_p} \quad (\text{A34})$$

and using Equation (A21) gives the following:

$$\mathcal{T}_2 \approx \mu_i I_i \quad (\text{A35})$$

Substituting Equations (A32) and (A35) into Equation (A23), the effective dynamics becomes:

$$\dot{I}_i \approx (1 - I_i - R_i) \sum_{j \in \mathcal{V}_2} \beta_{ij} I_j - \mu_i I_i \quad (\text{A36})$$

where:

$$\beta_{ij} = \frac{\sum_{p \in C_i} \sum_{q \in C_j} w_p \beta_{qp}}{\sum_{p \in C_i} w_p}, \quad \mu_i = \frac{\sum_{p \in C_i} w_p \mu_p}{\sum_{p \in C_i} w_p} \quad (\text{A37})$$

This completes the derivation of the effective parameters across scales 2 and 3. The general formulation relating the parameters of the SIR model across these scales is:

$$\beta_{ij} = \frac{\sum_{p \in C_i} \sum_{q \in C_j} w_q \beta_{pq}}{\sum_{q \in C_j} w_q}, \quad \mu_i = \frac{\sum_{p \in C_i} w_p \mu_p}{\sum_{p \in C_i} w_p} \quad (\text{A38})$$


TABLE A1 Summary of key variables used in Appendix A.

Variable	Description
S, I, R	Fractions of susceptible, infected, and recovered entities
i, j, p, q	Node indices for iterating in equations
β_{ij}	Transmission rate from node i to node j
μ_i	Recovery rate of node i
$\beta_{\text{eff}}, \mu_{\text{eff}}$	Effective infection/recovery rates at scale 1
w_i	Weight of node i , fraction of total entities it contains
C_n	Set of child nodes of node n
\mathcal{V}_l	Set of nodes at scale l ($l = 1, 2, 3$)
G_i	Total incoming transmission influence: $G_i = \sum_j \beta_{ji}$
g_{ji}	Normalized influence: $g_{ji} = \beta_{ji}/G_i$
N	Total number of nodes
I_i	Observed fraction of infected entities at node i and time t
\hat{I}_i	Model prediction for I_i

where $i, j \in \mathcal{V}_2$ represent nodes at scale 2, and $p \in C_i, q \in C_j$ represent their respective child nodes at scale 3.

Table A1 contains the description of the key variables used in Appendix A.

APPENDIX B: MULTISCALE NETWORK FOR CONGESTION MODEL

The multiscale network for the congestion model consists of five different scales. The geographical area under consideration is the San Francisco Bay Area, the whole of which is modeled as one single node in scale 1. The network at the other four scales is constructed based on Uber H3 Spatial Indexing System (H3 Geospatial Indexing System, 2018). Descriptive details of this multiscale network are presented in Table B1.

Each node has two parameters—its own recovery rate and self-infection rate—while each edge has a transmission rate parameter. Therefore, at any given scale, the total number of parameters equals the number of edges plus twice the number of nodes. Such a multiscale network using the H3 Spatial Indexing System leverages several of its key features, including the presence of hierarchi-

TABLE B1 Description of the five scales corresponding to the congestion model. The last column indicates the corresponding H3 resolution.

Scale	Nodes	Edges	Parameters	Area (km ²)	H3 Res.
1	1	1	2	18,000	3
2	9	36	54	1770	4
3	31	150	212	253	5
4	109	568	786	36	6
5	313	1797	2423	5	7

ALGORITHM 1 Construction of Uber H3 Hexagons for Traffic Congestion Analysis

- 1: Define the bounding box over all road links in the region.
- 2: Generate H3 hexagons to cover the bounding box.
- 3: **for** each hexagon h **do**
- 4: **if** h has no road link intersecting its edges **then**
- 5: Remove h .
- 6: **end if**
- 7: **end for**
- 8: **for** each hexagon h without any road links within it **do**
- 9: Merge h with its neighboring hexagon that contains the maximum number of road links.
- 10: **end for**
- 11: Assign red color to polygon edges intersected by road links.
- 12: Construct the adjacency matrix based on spatial connectivity of hexagons.

cal relationships between hexagons across different scales. While the hexagons are uniformly tessellated across space, a few hexagons contain only a few road links, and thus cause noisy variations in the congestion curve. To mitigate this issue, hexagons containing fewer road links than a threshold are aggregated with their neighboring hexagon containing the highest number of links. If there is a tie, the first polygon based on the fixed seed ordering in the network is chosen. This process is recursively applied to ensure that all polygons contain a sufficient number of links (Algorithm 1).

Two polygons in this revised network are connected via the adjacency matrix if there is a road-link connecting them, enabling the possibility of spread of traffic congestion. The L -smoothness value quantifies the temporal variation of a function $f(t)$ by summing the absolute differences between consecutive values over time. For a congestion curve $f(t)$, sampled at discrete time points t_1, t_2, \dots, t_n , the L -smoothness value is computed as:

$$L = \sum_{i=1}^{n-1} |f(t_{i+1}) - f(t_i)| \quad (\text{B39})$$

where n is the total number of time points. This computation is repeated for each geometry's congestion curve, producing a list of L -smoothness values.

Aggregation thresholds of 50, 100, 200 were tested. The most significant improvement in congestion curves is observed with a threshold of 50, while higher thresholds provide consistent but incremental benefits. The aggregation process notably improves the resolution-7 curves due to the high number of hexagons with few road links at this level. The data used for fitting the congestion model are aggregated according to the above algorithm to ensure each polygon has ≥ 200 road-links within it. Note that the



containment property of road-links within a polygon is defined based on the centroid of road-links. The key benefit of this aggregation process is most visible in the finest scale, where the average L-smoothness value of the congestion curves decreases by almost 8 orders of magnitude, thus reducing the noise in the data.

APPENDIX C: CONGESTION DATA GENERATION THROUGH TRAFFIC SIMULATIONS

Traffic in the San Francisco Bay Area is simulated using SUMO (Simulation of Urban Mobility; Lopez et al., 2018), Version 1.12.0, executed on a Linux system with x86_64 architecture and 24 CPUs. The implemented road network consists of over 196,000 links, and each complete simulation run requires approximately 6 h. The simulation parameters, including the routing algorithm and time window, are defined along with input data comprising the road network, OD demand, and Traffic Assignment Zone (TAZ) information.

The traffic demand between OD pairs is derived from prior work (Ambühl et al., 2023). As demand increases, the simulator teleports more vehicles to alternate links to break gridlock. This teleportation is triggered when vehicles become immobilized on a link due to severe congestion. This procedure calibrates the demand levels for the traffic simulations (Cornacchia et al., 2024).

APPENDIX D: WEIGHTED ADJACENCY MATRIX FOR INFECTION MODEL THROUGH TRIPS

For scale 2 of the infection model that represents various counties within California as nodes in the network, the directed edges were constructed based on the number of trips within and between the counties, as obtained from Replica (2024). This is representative of mobility and social contact as the key enabler of infection transmission in an epidemic simulation setting (Pardo-Araujo et al., 2023).

Consider the matrix A , element A_{ij} of which contains the number of trips from county i to county j . The probability distribution of the entries in this matrix as a function of the distance between the pair of counties is presented in Figure D1. The two annotations represent the trips between the counties of Los Angeles and San Bernardino as relevant in Figure 6, while the other represents the trips between the two major metropolitan counties of California, San Francisco and Los Angeles.

The (i, j) th entry of the outflow-normalized adjacency matrix \tilde{A} is defined as follows and is utilized during the model fitting process:

$$\tilde{A}_{ij} = \frac{A_{ij}}{\sum_k A_{ik}} \quad (\text{D40})$$

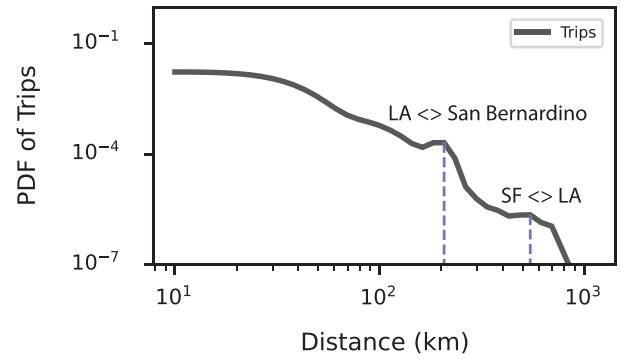


FIGURE D1 Probability distribution of trips between counties in California. LA and SF refer to the abbreviations for the counties of Los Angeles and San Francisco, respectively.

Here, $\sum_k A_{ik}$ represents the sum of all trips originating from county a , ensuring that each row of \tilde{A} sums to 1, thus normalizing the outflow from each county.

APPENDIX E: MODEL FITTING PROCESS AND REGULARIZATION TERMS FOR MULTISCALE NETWORKS

The model fitting process is formulated as an optimization problem, aiming to minimize the MSE between the observed data and the model's predictions. These predictions are obtained by integrating the differential equations of the SIR model using appropriate parameters. Implemented in Python, the fitting procedure involves solving for the optimal parameters β and μ that best align the model's output with the data at a given scale. The corresponding objective function is defined as follows:

$$E(\theta) = \sum_{i=1}^N \sum_{t=1}^T (I_{i_t} - \hat{I}_{i_t}(\theta))^2 + \lambda \|\theta\|^2 \quad (\text{E41})$$

The L-BFGS optimization method is invoked to solve for the optimal parameters. Two stopping conditions are implemented, based on if either the error tolerance decreases beyond a certain threshold, or if the number of epochs for which the optimization has run exceeds a preset value. Furthermore, this process is repeated for 200 independent iterations, to ensure that the optimal parameters are indeed the global minimum and are not an artifact of the optimization process, which can happen when the algorithm get stuck in a local minimum.

The proposed framework is integrated into the model through the regularization terms. The parameters of a scale containing a network description of the system are related to the scale representing the whole system as a single node through the following expressions:

$$\beta_{\text{eff}} \approx \sum_{i,j \in C_{n_1}} w_i \beta_{ji}, \quad \mu_{\text{eff}} \approx \sum_{i \in C_{n_1}} w_i \mu_i \quad (\text{E42})$$

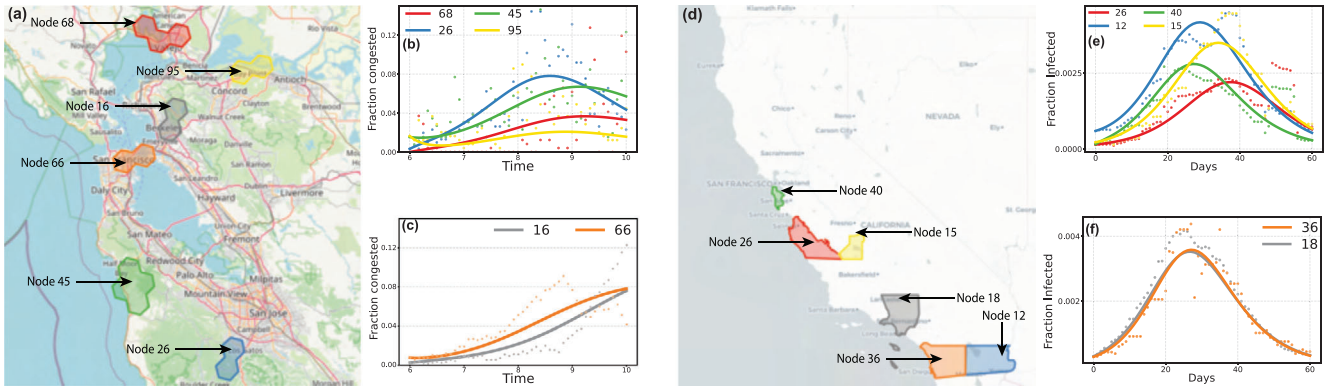


FIGURE E1 Spatial context and model fits for selected nodes. (a) Map of two annotated outliers from Figure F1a and the four highest RMSE congestion nodes; (b) congestion–model fits for the four highest RMSE nodes; (c) congestion–model fits for the two annotated nodes; (d–f) analogous panels for the infection model.

Furthermore, the parameters corresponding to two scales, both of which contain a network description of the system with multiple nodes, are related through the following equations;

$$\beta_{ij} \approx \frac{\sum_{\substack{p \in C_i \\ q \in C_j}} w_q \beta_{pq}}{\sum_{q \in C_j} w_q}, \quad \mu_i \approx \frac{\sum_{p \in C_i} w_p \mu_p}{\sum_{p \in C_i} w_p} \quad (\text{E43})$$

Equations (E42) describing the mathematical relationship between the parameters corresponding two different scales, one of which models the whole system through a single node, can be incorporated into the objective function of the corresponding optimization problem through a regularization-based approach:

$$E(\theta) = \sum_{i=1}^N \sum_{t=1}^T (I_{i_t} - \hat{I}_{i_t}(\theta))^2 + \lambda_\beta \left(\beta_{\text{eff}} - \sum_{i=1}^N \sum_{j=1}^N w_i \beta_{ji} \right)^2 + \lambda_\mu \left(\mu_{\text{eff}} - \sum_{i=1}^N w_i \mu_i \right)^2 + \lambda \|\theta\|^2 \quad (\text{E44})$$

Similarly, Equation (E43), which approximates the mathematical relationship between the parameters corresponding to two different scales—both of which have a network representation of the system with multiple nodes—can be incorporated into the objective function as below:

$$E(\theta) = \sum_{i=1}^N \sum_{t=1}^T (I_{i_t} - \hat{I}_{i_t}(\theta))^2 + \lambda_\beta \left(\beta_{ij} - \frac{\sum_{\substack{p \in C_i \\ q \in C_j}} w_q \beta_{pq}}{\sum_{q \in C_j} w_q} \right)^2 + \lambda_\mu \left(\mu_i - \frac{\sum_{p \in C_i} w_p \mu_p}{\sum_{p \in C_i} w_p} \right)^2 + \lambda \|\theta\|^2 \quad (\text{E45})$$

$$+ \lambda_\mu \left(\mu_i - \frac{\sum_{p \in C_i} w_p \mu_p}{\sum_{p \in C_i} w_p} \right)^2 + \lambda \|\theta\|^2 \quad (\text{E45})$$

Thus, if the model is fit without the implementation of regularization at any given scale, the model is based on the objective function as described in Equation (E41). When the regularization approach is implemented, the model uses Equation (E44) for fitting the first scale representing a network description of the system. For scales that are finer, the objective function used during the fitting process is that described in Equation (E45).

APPENDIX F: LIMITATIONS IN THE MODELING FRAMEWORK

In both the congestion and infection models, model-fit errors tend to be lower for higher weight nodes, likely because observations for those nodes are less noisy. Figure F1 shows, for the congestion and infection models, respectively, scatter plots of per-node RMSE versus the standardized weight $z(w_i) = (w_i - \bar{w})/\sigma_w$. Two nodes

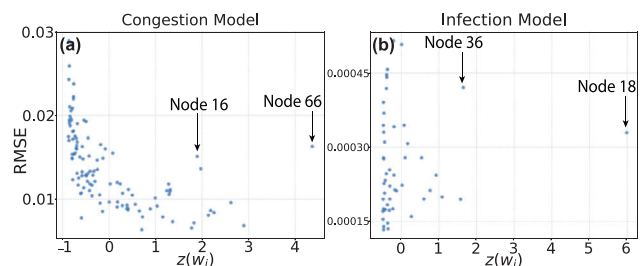


FIGURE F1 RMSE versus standardized node weight. (a) Congestion model; (b) infection model. Each point is a node; the x -axis is $z(w_i) = (w_i - \bar{w})/\sigma_w$ and the y -axis is per-node RMSE. Annotated indices denote nodes examined in Figure E1.



in each subfigure are annotated by index; Their spatial locations and time-series fits are examined in Figure E1.

Figure E1 summarizes spatial context and model fits for selected nodes. Panel (a) maps the two annotated outlier nodes from Figure F1a together with the four congestion-model nodes with the highest RMSE across the San Francisco Bay Area; panel (b) shows the model fits for those four congestion nodes; panel (c) shows the fits for the two annotated congestion nodes. Panels (d–f)

present the analogous results for the infection model. In the congestion model, the four highest RMSE nodes have very low weight and are located in more rural areas with fewer road links. The two annotated exceptions in Figure F1a lie in urban areas with higher weights, but still exhibit relatively high RMSE due to non-SIR-like congestion trajectories. For the infection model, elevated RMSE at some nodes is primarily driven by observational noise.